Supporting Information

Binding Modes of Thioflavin T and Congo Red to the Fibril Structure of Amyloid-β(1–42)

Benedikt Frieg[a,b], Lothar Gremer[b,c], Henrike Heise[b,c], Dieter Willbold[b,c], Holger Gohlke[a,b,d*]

[a] John von Neumann Institute for Computing (NIC), Jülich Supercomputing Centre (JSC), Forschungszentrum Jülich GmbH, Jülich, Germany.

[b] Institute of Biological Information Processing (IBI-7: Structural Biochemistry), Forschungszentrum Jülich GmbH, Jülich, Germany.

[c] Institut für Physikalische Biologie, Heinrich Heine University Düsseldorf, Düsseldorf, Germany.

[d] Institute for Pharmaceutical and Medicinal Chemistry, Heinrich Heine University Düsseldorf, Düsseldorf, Germany.

Table of Content

Supplemental Methods

System preparation and simulation procedure

To investigate fluorescent dye-binding to the Aβ(1-42) fibril, we performed unbiased MD simulations of THT and CR in the presence of the Aβ(1-42) fibril[1]. Initial coordinates for the Aβ(1-42) fibril structure were taken from the cryo-EM structure (PDB ID 5OQV [1]). We prepared two structural models of the Aβ(1-42) fibril structure, either composed of ten or 20 Aβ(1-42) periodically arranged peptide chains. For phenylalanine 20 (F20; following the one-letter nomenclature) two rotamers are reported in the 3D structure[1], with the F20 side chain oriented towards V18 or towards E22. We kept the rotamer with the F20 side chain oriented towards V18, anticipating favorable interactions between V18 and F20. The protonation states of all titratable residues of the fibril at pH 2 were resolved by NMR spectroscopy and incorporated in our setup (Table S3). That way, the protonation states in the simulations match those in *in vitro* experiments. THT and CR were also prepared for pH 2 using Epik distributed with the Maestro suite of programs [2, 3] to calculate the pK_a of relevant functional groups. The predicted protonation states of THT and CR are shown in **Figure S1**. 3D structures of THT and CR were subjected to quantum mechanical (QM) geometry optimization at the HF/6-31G* level of theory using Gaussian 16[4]. The QM-optimized 3D structures were used for subsequent binding simulations. To do so, we randomly placed one dye molecule and one of the structural models of the Aβ(1-42) fibril structure, composed by either ten Aβ(1-42) peptides in the case of THT or 20 Aβ(1-42) peptides in the case of CR, into an octahedral box using PACKMOL[5]. The systems were neutralized and solvated with chloride atoms and TIP3P[6] water, respectively, using LEaP[7] of Amber16[8]. For each dye, we prepared 45 different initial configurations, in which the initial distance between the dye molecule and the Aβ(1-42) fibril ranged from 13 Å to 62 Å.

We used the Amber ff14SB force field[9] to describe the Aβ(1-42) fibril and the GAFF force field[10] to describe the dye molecules. For the dye molecules, atomic partial charges were derived according to the RESP procedure[11, 12]. As to THT, this force field-charge combination was successfully applied in a previous study[13], and the THT structure after molecular mechanics (MM) minimization matched the QM-minimized structure. As to CR, however, the MM-minimized structure showed a significant rotation around the diazo groups leading to a ladder-like orientation of the aromatic rings, whereas the aromatic rings were almost coplanar in the QM-optimized structure. Hence, we derived new force field parameters for the respective

torsion following ref.[14]. With the optimized force field parameters, the CR structure after MM minimization matched the QM-minimized structure (**Figure S10**).

The exact minimization, thermalization, and equilibration protocol is reported in ref.[15], which was already applied previously to study ligand binding processes [16, 17]. In short, all systems were initially subjected to three rounds of energy minimization to resolve bad contacts. Subsequently, systems were heated to 300 K, and the pressure was adapted such that a density of 1 g/cm^3 was obtained. During thermalization and density adaptation, we kept the solute fixed by positional restraints of 1 kcal mol^{-1} Å^{-2}, which were gradually removed. Subsequently, the systems were subjected to unbiased production simulations of 1 μs length each, to study THT and CR binding to the Aβ(1-42) fibril. The simulations were not biased by any prior information on potential binding epitopes.

All minimization, equilibration, and production simulations were performed with the *pmemd.cuda* module[18, 19] of Amber16[8] on JUWELS[20]. During production simulations, we set the time step for the integration of Newton's equation of motion to 4 fs according to the hydrogen mass repartitioning strategy[21]. Coordinates were stored into a trajectory file every 200 ps. The procedure results in 5000 configurations for each production run that were considered for subsequent analyses.

Determination of the binding mode models

During visual inspection of the MD trajectories, we observed multiple binding and unbinding events of the dye molecules to and from the Aβ(1-42) fibril. Thus, we initially determined all stably bound dye poses by calculating the RMSD of the dyes with respect to the previous configuration after superimposing the Aβ(1-42) fibril structure, using *cpptraj*[22]. That way, the RMSD becomes a measure for the spatial displacement of a dye molecule between two snapshots. THT poses with RMSD < 1.2 Å and CR poses with RMSD < 1.0 Å, respectively, were defined as stably bound.

Beforehand, we calculated the mean square displacement $<\Delta^2 r(t)>$ of THT and CR to estimate the spatial displacement for free diffusive motion, according to eq. (S1)

$$<\Delta^2 r(t)> \sim 6\, Dt\,, \qquad \text{(S1)}$$

where D is the diffusion coefficient (THT in methanol solution at 30 °C: $D = 7.8 \pm 0.03 * 10^{-10}$ m^2/s [23]; CR in D_2O at 30 °C: $D = 1.95 * 10^{-10}$ m^2/s [24]), and t = 200 ps, the time interval of

saving atomic positions into a trajectory file. Note that eq. (S1) is only valid if $t >> t_c$ (t_c: molecular correlation time); this is given here as former studies revealed for THT t_c = 0.4 ps[25] and for CR t_c = 0.2 ps[26], measured in water. Solving eq. (S1), thus, yields for THT $\sqrt{<\Delta^2 r(t)>}$ = 9.64 Å and for CR $\sqrt{<\Delta^2 r(t)>}$ = 4.89 Å. RMSD values smaller than $\sqrt{<\Delta^2 r(t)>}$ thus arise from restrictions of diffusive motions of the dye molecule during the MD simulations, which, in this case, can be explained by complex formation with the Aβ(1-42) fibril.

The stably bound poses (**Figure S4**) were subjected to clustering using the hierarchical agglomerative (bottom-up) algorithm as implemented in *cpptraj*[22, 27], using the minimum distance ε between the clusters as cluster criterion. Starting from ε = 2.0 Å, we gradually increased ε in 0.5 Å intervals until the population of the largest cluster remained unchanged (ε_{THT} = 5.0 Å and ε_{CR} = 4.5 Å). The resulting cluster fractions are shown in **Figure S11**.

Additionally, we calculated 3D density grids over the complete ensemble (45 × 1 µs), representing the probability density of the dye position relative to the centered fibril structure, using *cpptraj*[22]. To sharpen the distribution, we only considered the two carbon atoms connecting the two (central) rings in THT and CR. The resulting densities were normalized to the number of considered conformations, which are identical in both cases. For visualization purposes in Figures 2A and 3A, we only show regions with a probability density > 1/100 of the maximum value across the full density grid.

Molecular mechanics generalized Boltzmann surface area (MM-GBSA) calculations

The ten most highly populated clusters were considered for binding free energy calculations, performed with the MMPBSA.py[28] program of Amber16[8]. In the MM-GBSA calculations, the free energy of a molecule G_{mol} is calculated as the sum of gas-phase energies E_{MM} and solvation free energies G_{solv}, together denoted as effective energies, G_{eff}, and the configurational entropy S [29-33], with T being the absolute temperature (eq. (S2))

$$G_{mol} = E_{MM} + G_{solv} - TS \, . \tag{S2}$$

Binding energies ΔG_{bind} were computed according to eq. (S3)

$$\Delta G_{bind} = G_{complex} - G_{receptor} - G_{ligand} \, , \tag{S3}$$

where snapshots of the complex (Aβ + dye), receptor (Aβ), and ligand (dye) are obtained from MD simulations following the 1-trajectory approach[34]. Contributions due to changes in the configurational entropy of the ligand or the receptor upon complex formation were calculated

by normal mode analyses (NMA). Because NMA is computationally expensive, the entropic contributions were calculated for only every 10th snapshot in each cluster.

To compare the computed with experimentally determined binding affinities, we converted ΔG_{bind} into the standard free energy of binding ΔG^0_{bind} according to eq. (S4)[35], as done previously[29]. This takes into account that translational entropy depends on solute concentration[36, 37], leading to the concentration dependence of chemical equilibria that do not conserve the number of molecules (such as binding reactions)[38, 39].

$$\Delta G^0_{bind} = \Delta G_{bind} + R \cdot T \ln \frac{C^{ideal}}{C^0} , \quad \text{(S4)}$$

where R is the universal gas constant (R = 0.001987 kcal K^{-1} mol^{-1}), T = 298.15 K, C^0 is the standard state concentration of 1 mol l^{-1}, and C^{ideal} the ligand concentration of 0.041 mol l^{-1}, derived from the general gas equation at a pressure of 101,325 Pa and a temperature of 298.15 K[40]. ΔG^0_{bind} is directly related to the dissociation constant K_D according to eq. (S5)

$$\Delta G^0_{bind} = R \cdot T \ln (K_D) . \quad \text{(S5)}$$

K_D values derived from computations according to eq. (S2) - (S5) are denoted as K_D^{comp} and are compared with experimental values K_D^{exp} (or K_i^{exp}). The total standard error of the mean of the computations, denoted as SEM_{total}, is estimated following the principles of Gaussian error propagation according to eq. (S6)

$$SEM_{total} = \sqrt{(SEM_{G_{eff}})^2 + (SEM_{TS})^2} , \quad \text{(S6)}$$

where $SEM_{G_{eff}}$ and SEM_{TS} are the SEMs from MM-GBSA and NMA computations, respectively. The results from binding free energy calculations are reported as $\Delta G^0_{bind} \pm SEM_{total}$. In addition to K_D^{comp}, we also computed the upper and lower limits of K_D^{comp} considering the uncertainties of our computations, by inserting either $\Delta G^0_{bind} + SEM_{total}$ or $\Delta G^0_{bind} - SEM_{total}$ into eq. (S5).

Determination of intramolecular mobility

To investigate whether the intramolecular mobility of the aromatic rings relative to each other is reduced in the proposed binding models, which is a structural prerequisite for a dyo to fluoresce[41], we additionally performed five replica of MD simulations of 1 µs length each of either THT or CR in the absence of the Aβ(1-42) fibril. Other than that, the simulation protocol

remained unchanged to the one used for simulating dye binding. As a measure for intramolecular mobility, we determined the dihedral angle defined between the aromatic rings in both dyes (see inlets in **Figure S5** and **Figure S7**). The same dihedral was also calculated for all dye poses in a cluster considered bound to the Aβ(1-42) fibril. The results are visualized as a histogram (normalized to the sum of all bins) in **Figure S5** and **Figure S7** In all bound poses, the intramolecular mobility is reduced compared to the mobility of the dye in solution.

Determination of fibril stability

To investigate whether the protonation states according to pH 2[1] or the presence of the fluorescent dyes alter the fibril structure, we performed ten replica of MD simulations of 1 μs length each of the Aβ(1-42) fibril in the absence of the dyes. The replica simulations were prepared following the protocol in ref.[15]. Other than that, the simulation protocol remained unchanged to the protocol of dye binding. To evaluate the structural integrity of the fibril, we calculated the backbone root mean square deviation (RMSD) relative to the cryo-EM structure[1] that served as the starting structure. The same analysis was performed for the fibril structure in the presence of the dyes. The results are expressed as average RMSD ± SEM (**Figure S9**). As the SEM is almost equal in all cases also the variances can be considered as equal, such that a *t*-test was performed, and *p*-values < 0.05 were considered significant.

Supplemental Figures

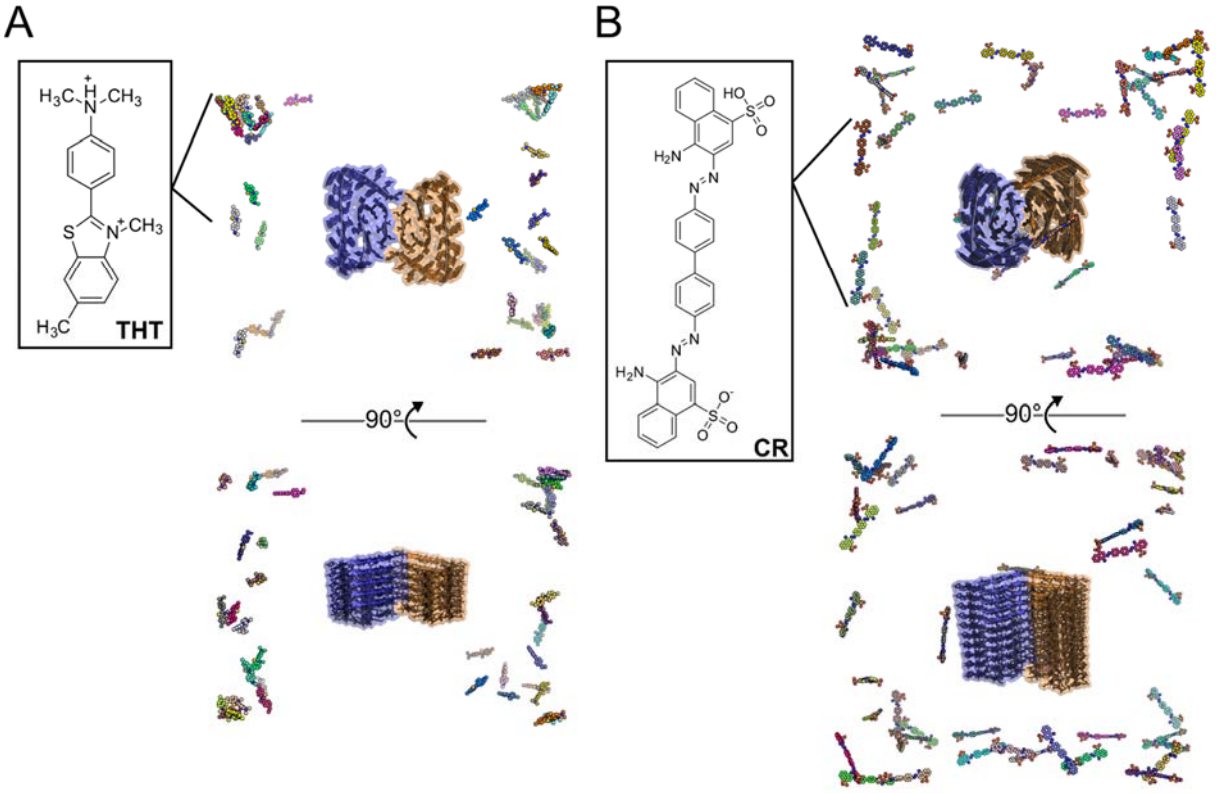

Figure S1: 45 independent starting configurations for dye binding simulations.
Differently colored starting positions of Thioflavin-T (THT) (**A**) and Congo red (CR) (**B**) molecules around the structural models of the Aβ fibril; from each starting position, an independent binding simulation was performed for 1 μs length. The blowups show structural formulas of the dye molecules. The protofilaments of the Aβ fibril are colored differently.

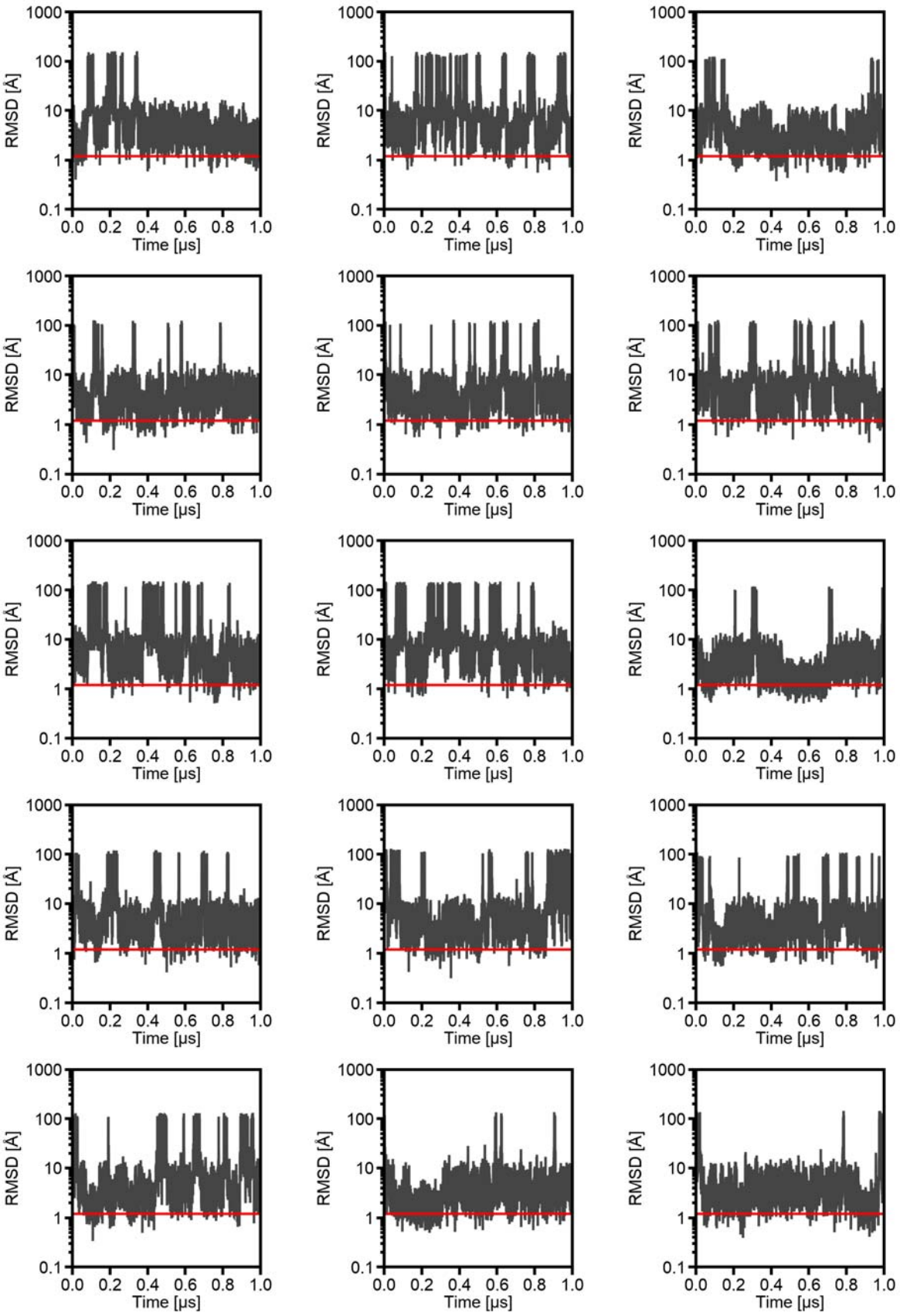
RMSD [Å]
1000
100
10
1
0.1
0.0 0.2 0.4 0.6 0.8 1.0
Time [μs]

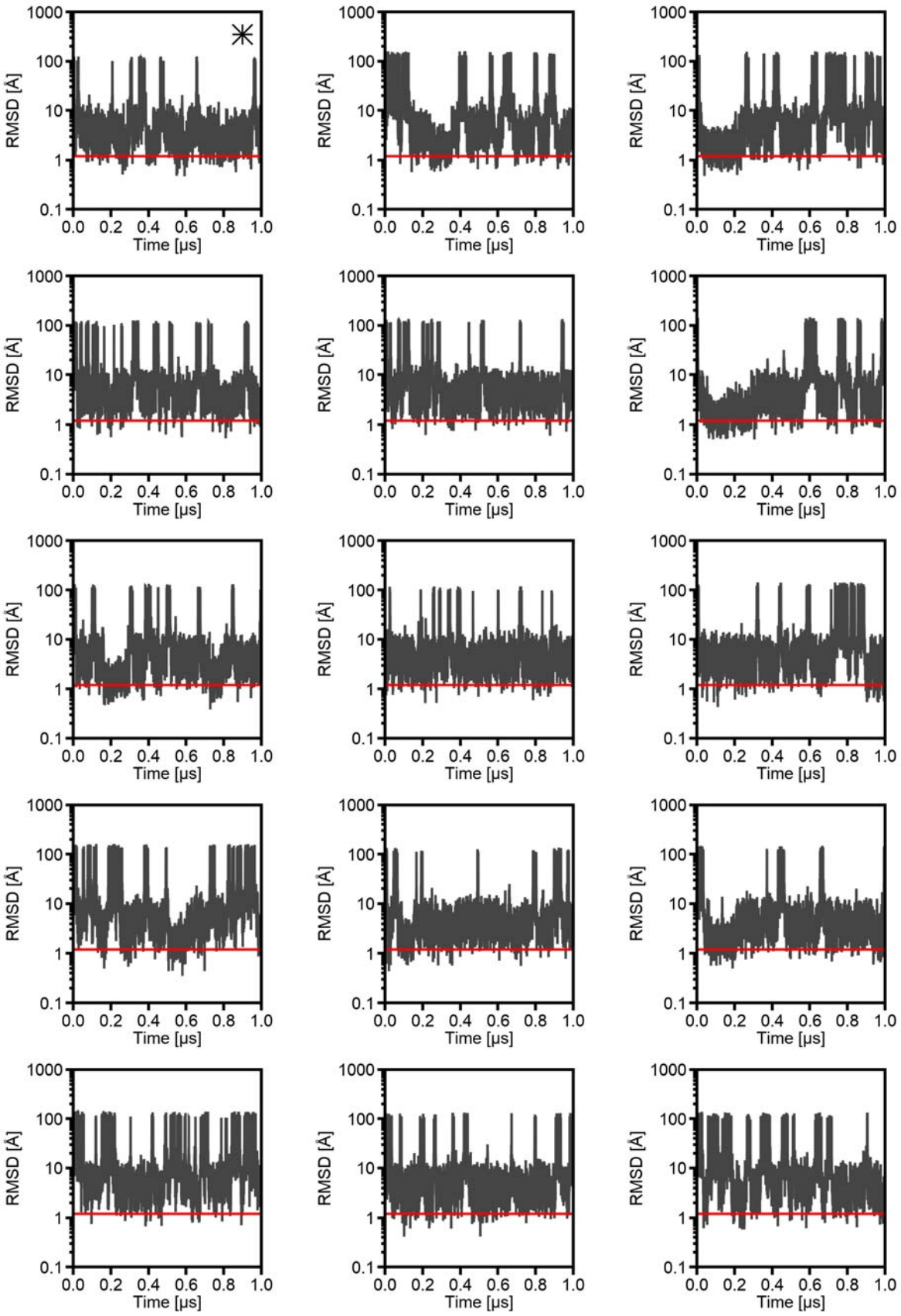
RMSD [Å]
1000
100
10
1
0.1
0.0 0.2 0.4 0.6 0.8 1.0
Time [μs]

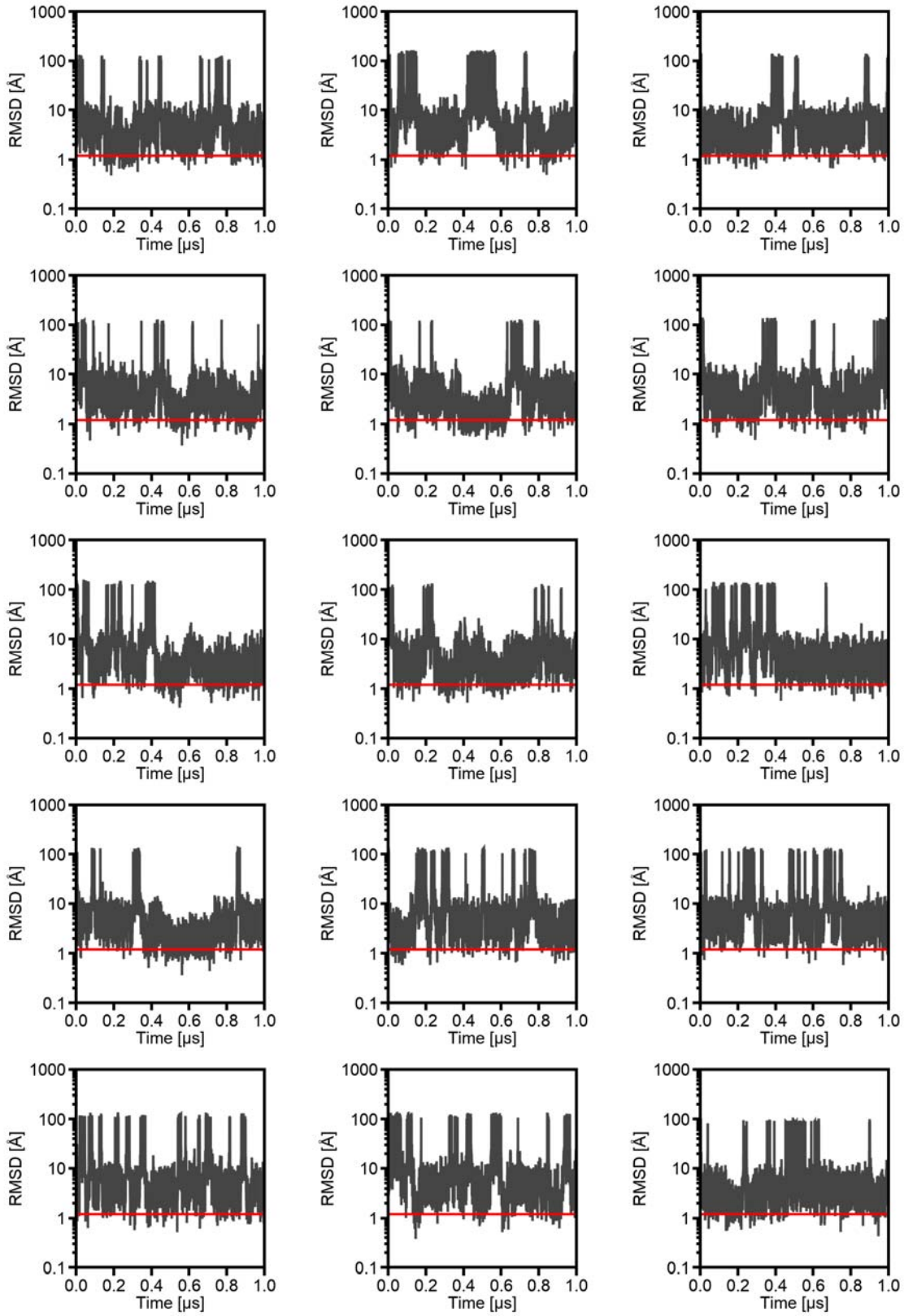

Figure S2: RMSD time series throughout MD simulations of THT binding.
The plots show the root mean square deviations (RMSD) throughout molecular dynamics (MD) simulations of 1 µs length. The RMSD was calculated for all non-hydrogen atoms in Thioflavin-T (THT) between two consecutive THT conformations after superimposing the fibril structure. That way, the RMSD becomes a measure for the spatial displacement between two THT conformations. THT is considered stably bound, if the RMSD < 1.2 Å (indicated by the red line). The Y-axis is scaled logarithmically. The representative trajectory shown in Movie S1 is marked by an "*".

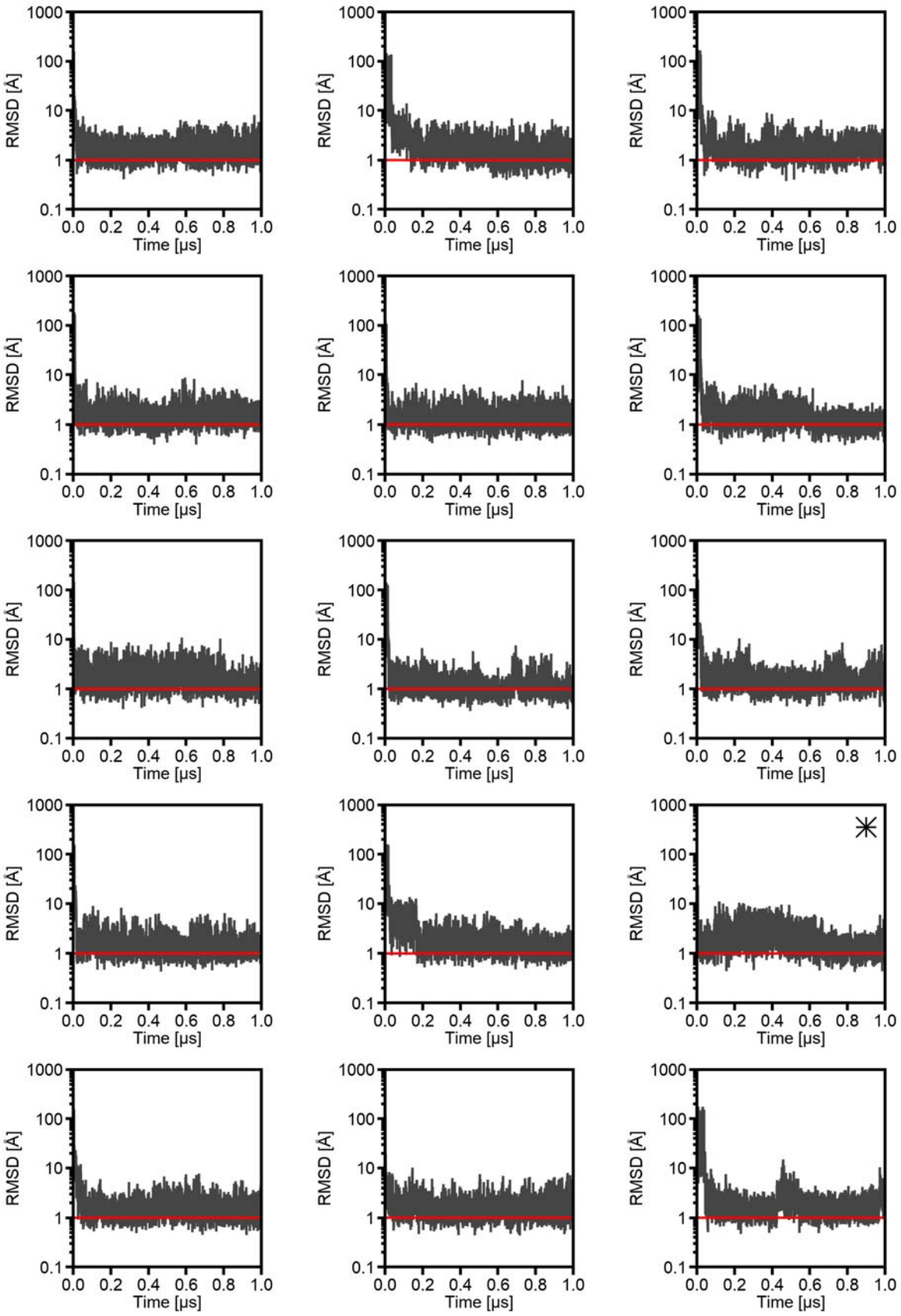
RMSD [Å]
Time [μs]
1000
100
10
1
0.1
0.0
0.2
0.4
0.6
0.8
1.0

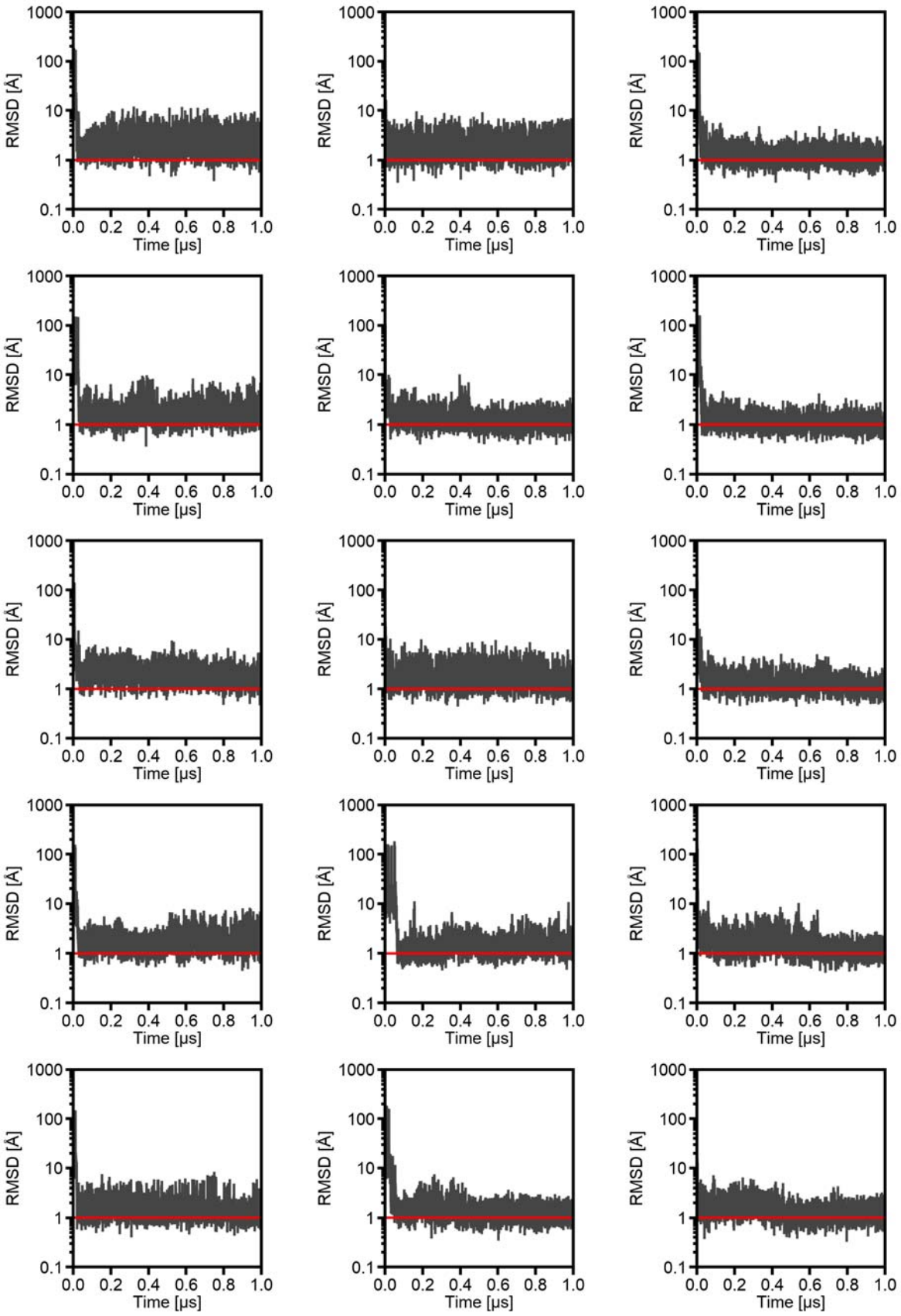
RMSD [Å]
1000
100
10
1
0.1
0.0 0.2 0.4 0.6 0.8 1.0
Time [μs]

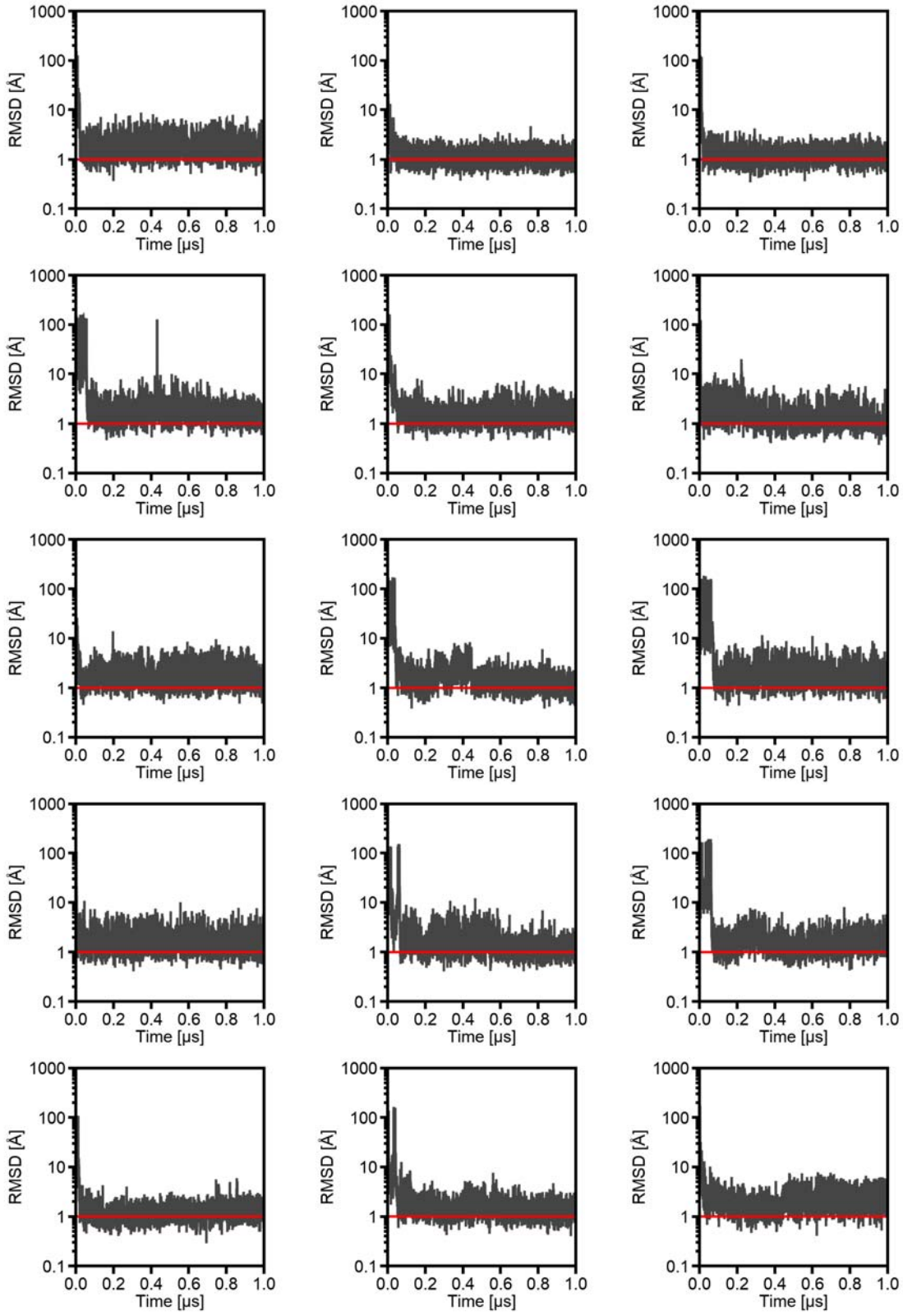

Figure S3: RMSD time series throughout MD simulations of CR binding.
The plots show the root mean square deviations (RMSD) throughout molecular dynamics (MD) simulations of 1 µs length. The RMSD was calculated for all non-hydrogen atoms in Congo red (CR) between two consecutive CR conformations after superimposing the fibril structure. That way, the RMSD becomes a measure for the spatial displacement between two CR conformations. CR is considered stably bound, if the RMSD < 1.0 Å (indicated by the red line). The Y-axis is scaled logarithmically. The representative trajectory shown in Movie S1 is marked by an "*".

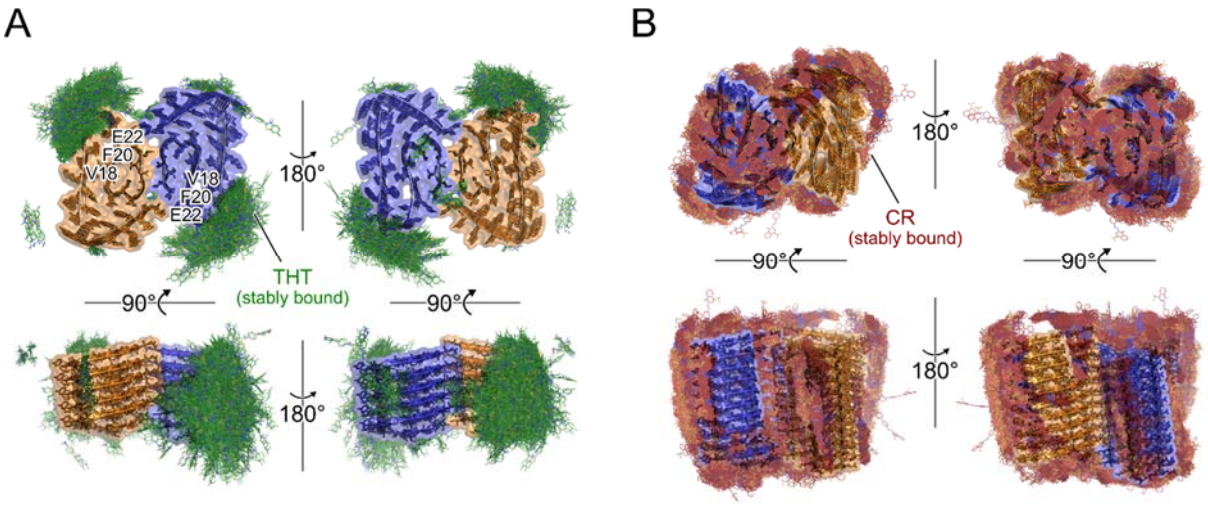

Figure S4: Stably bound dye poses.
Overlay of (**A**) Thioflavin-T (THT, green sticks) and (B) Congo red (CR, red sticks) bound to the Aβ(1-42) fibril (blue-orange cartoon-surface representation). THT and CR structures were extracted from 45 trajectories. All stably bound dye poses were considered for a similarity clustering.

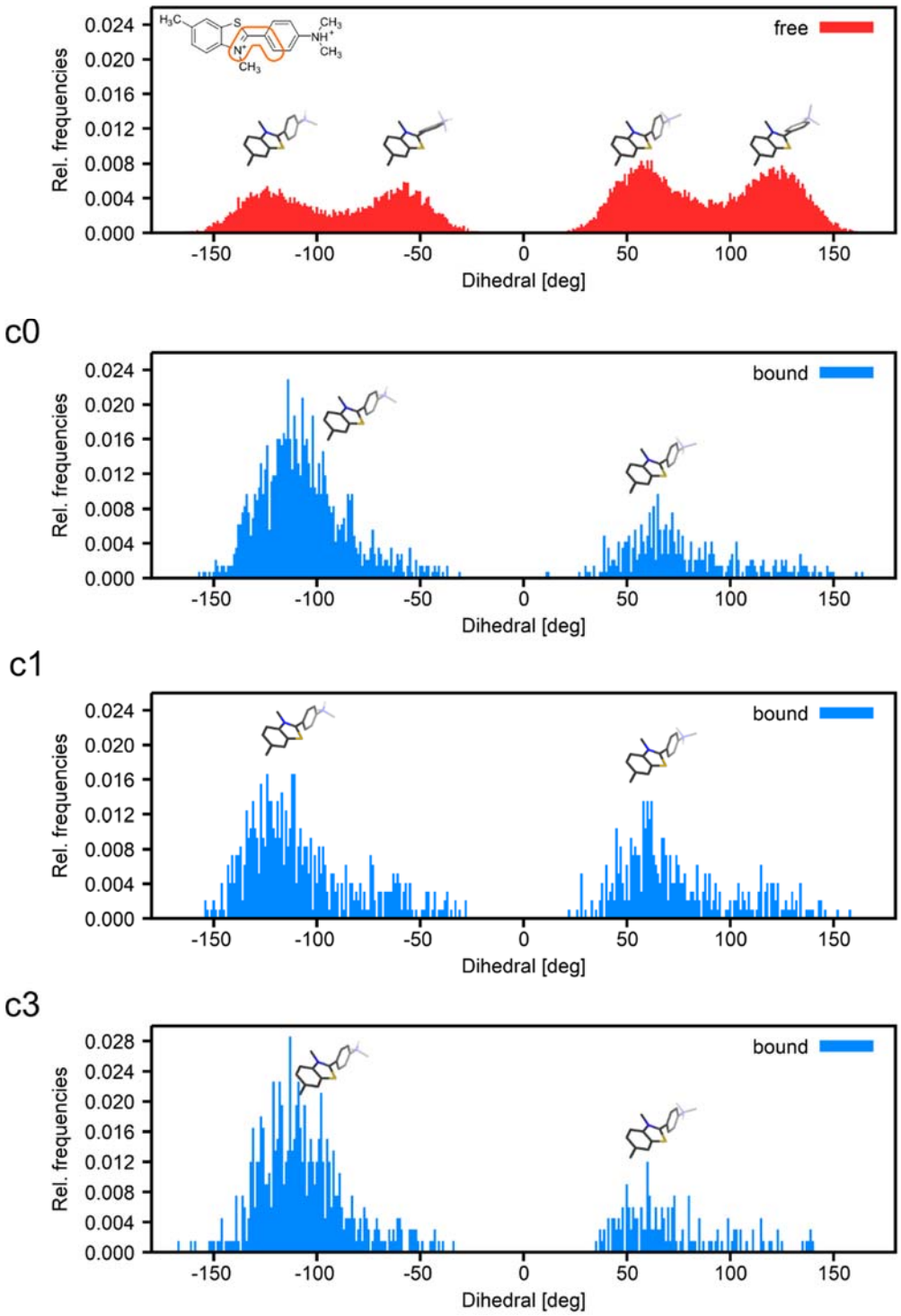

Figure S5: Analysis of the intramolecular mobility of Thioflavin T.
Histograms (bin size 0.1°) of the dihedral angle characterizing the relative orientation of the two rings of Thioflavin T (THT) in solution in the absence of the fibril (red histogram, top panel) and in the fibril-bound states c0, c1, and c3 (blue histograms). The four atoms defining the dihedral angle are marked by an orange frame in the structural formula of THT in the upper left corner of the top panel. The red histogram was calculated for 5 × 1 μs MD simulations of THT in the absence of the fibril. The blue histograms were calculated for all conformations in the clusters c0, c1, and c3, respectively, in which THT is bound to the fibril. THT conformations representing the individual maxima of the distributions are shown as stick models. All histograms are normalized to the sum of all bins.

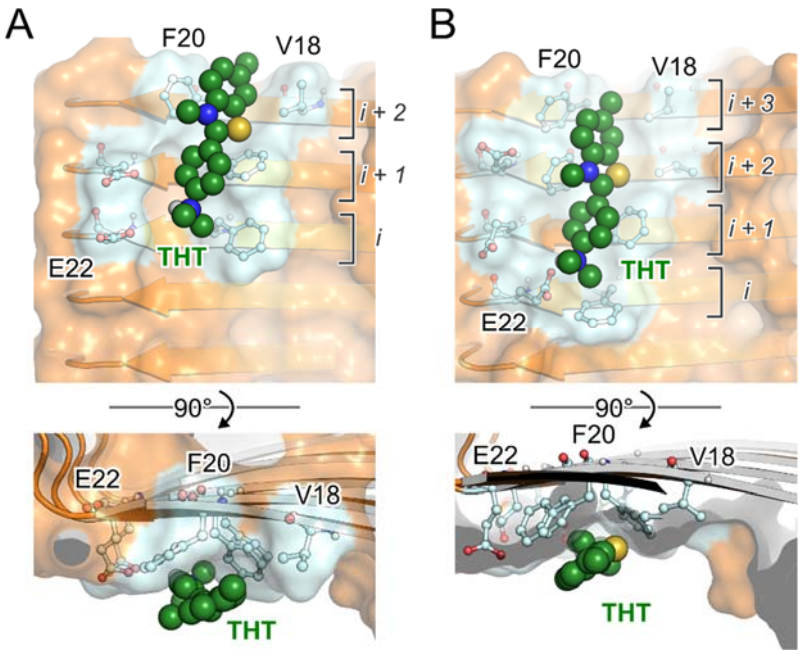

Figure S6: Predominant binding poses of Thioflavin-T.
Representative binding poses of Thioflavin-T (THT, green sphere model) extracted from cluster c1 (**A**) and c3 (**B**) (see also Table S1). In contrast to the energetically preferred orientation of THT (see Main Text Figure 2B), in A, THT binds to three stacked Aβ peptides, such that the methyl group is completely solvent-exposed, and in **B**, THT is slightly shifted to the upper edge of the fibril, such that the F20 side chain in position *i* is flipped. Residues with at least one atom within 4 Å of THT are colored cyan and depicted as ball-stick model. The remaining amino acids of the Aβ(1-42) fibril are colored orange. Panels at the bottom were rotated by 90° relative to the ones at the top.

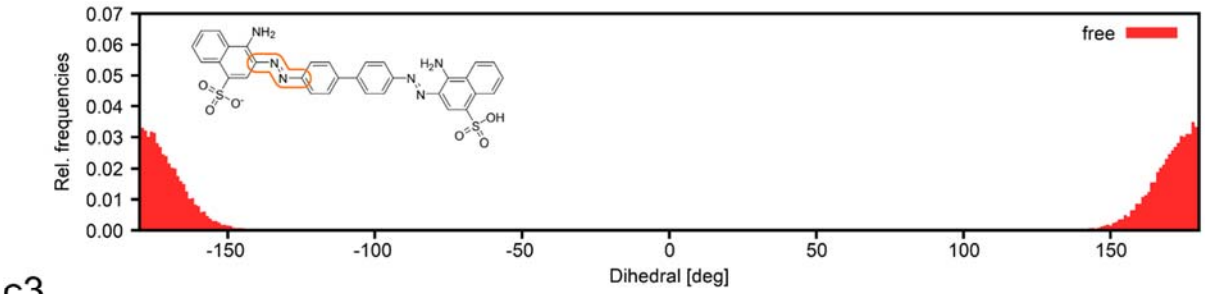
free
Rel. frequencies
Dihedral [deg]

c3

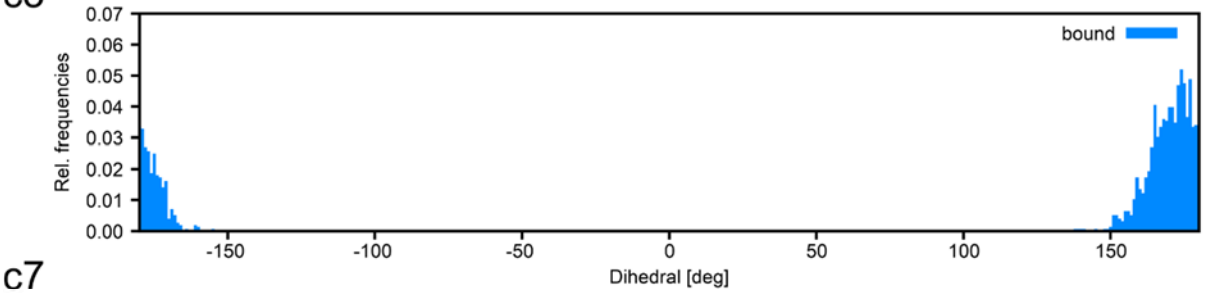
bound
Rel. frequencies
Dihedral [deg]

c7

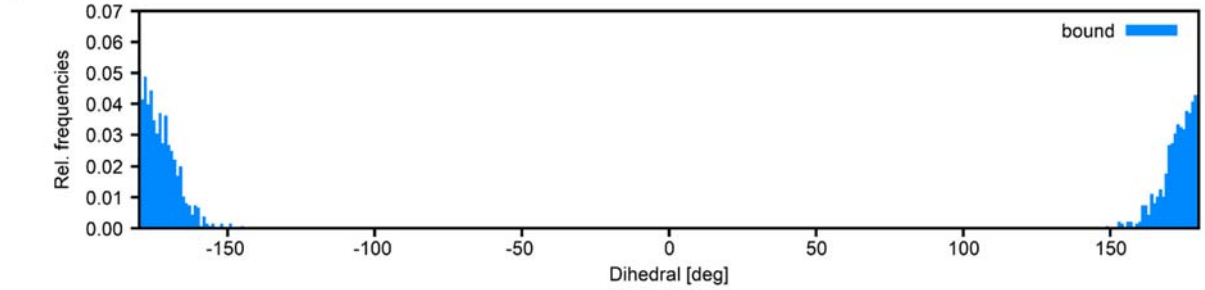
bound
Rel. frequencies
Dihedral [deg]

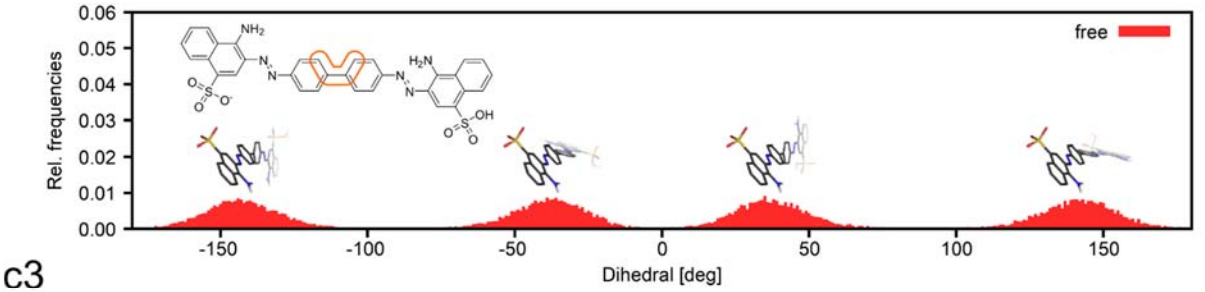
free
Rel. frequencies
Dihedral [deg]

c3

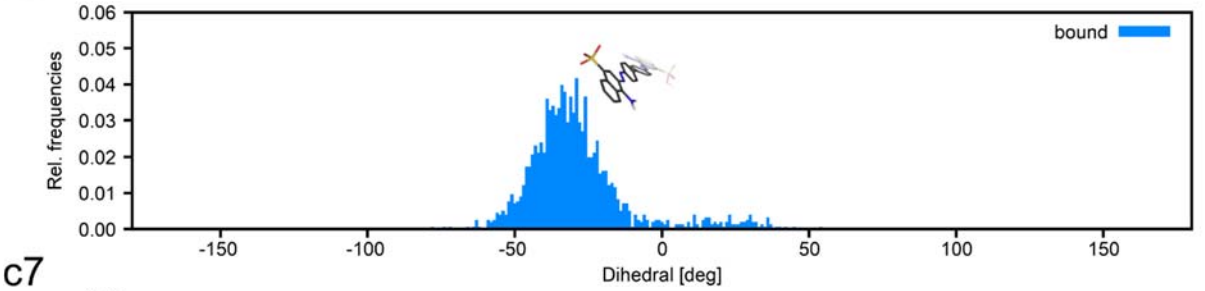
bound
Rel. frequencies
Dihedral [deg]

c7

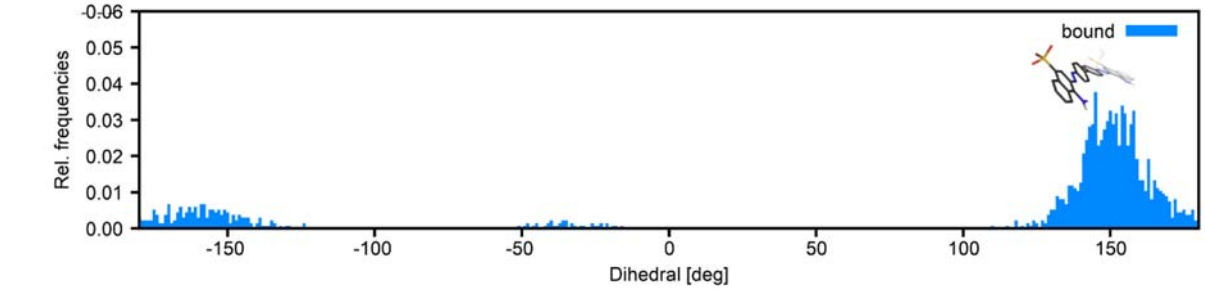
bound
Rel. frequencies
Dihedral [deg]

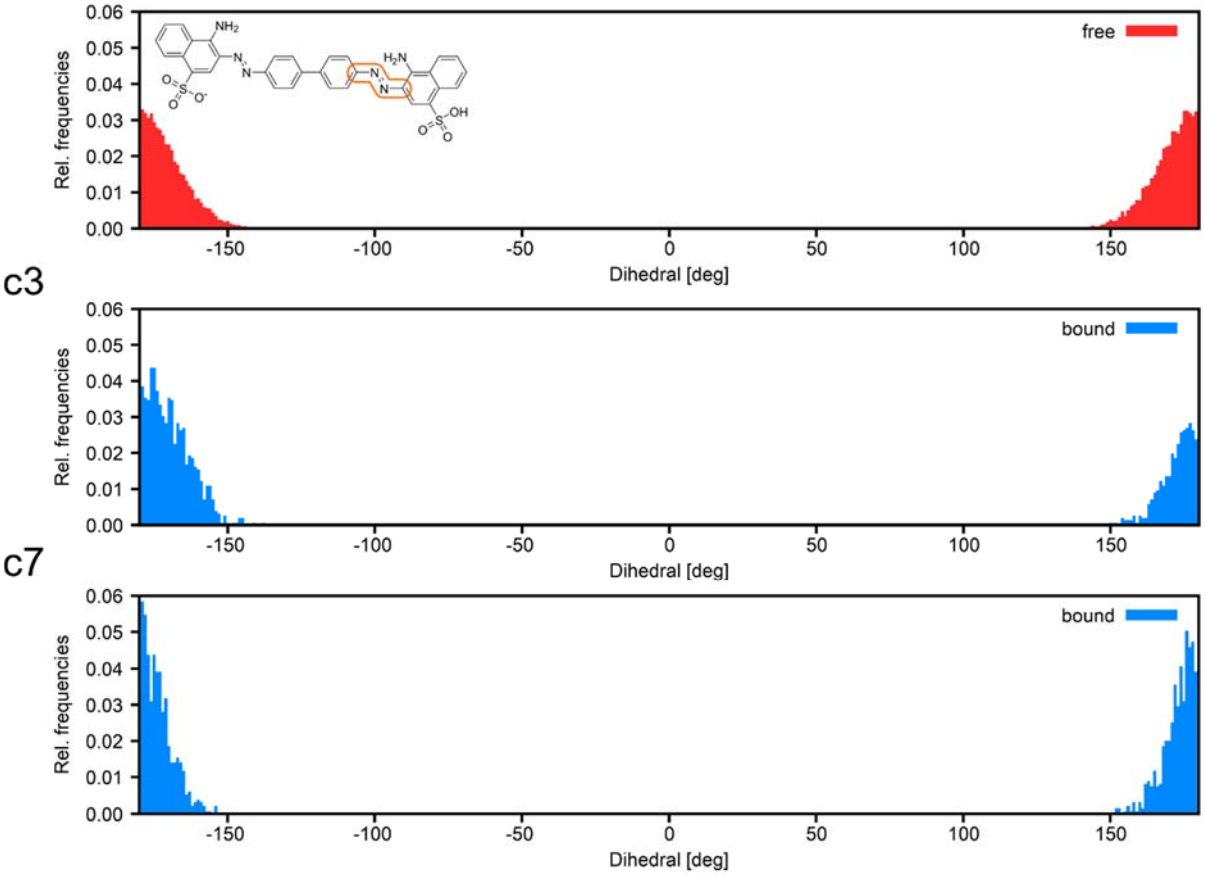

Figure S7: Analysis of the intramolecular mobility of Congo red.
Histograms (bin size 0.1°) of the dihedral angle characterizing the relative orientation of the rings of Congo red (CR) in solution in the absence of the fibril (red histograms) and in the fibril-bound states c3 and c7 (blue histograms). The four atoms defining the respective dihedral angle are marked by an orange frame in the structural formula of CR in the upper left corner of the plots. The red histograms were calculated for 5 × 1 µs MD simulations of CR in the absence of the fibril. The blue histograms were calculated for all conformations in the clusters c3 and c7, respectively, in which CR is bound to the fibril. CR conformations representing the individual maxima of the distributions are shown as stick models. All histograms are normalized to the sum of all bins.

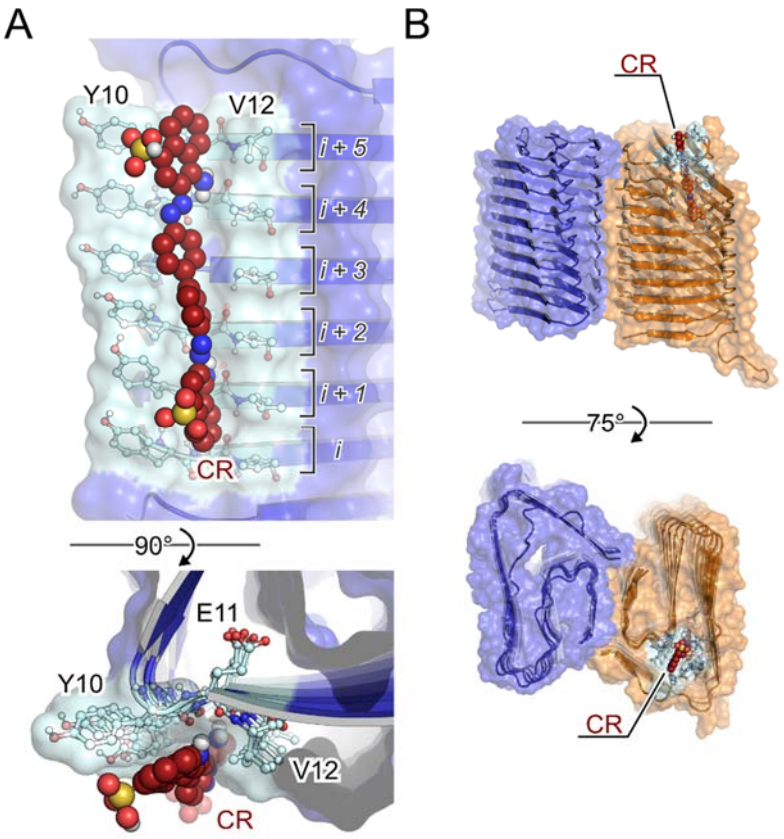

Figure S8: Predominant binding poses Congo red.
Representative binding poses of Congo red (CR, red sphere model) extracted from c7 (**A**) and c4 (**B**) (see also Table S2). In contrast to the energetically preferred orientation of CR (see Main Text Figure 3B), in A, CR is slightly twisted around the central C-C bond and flipped by 180°, such that the protonated sulfonic acid is oriented to the upper edge of the fibril. In B, CR is partially intercalated into one of the protofilaments. Residues with at least one atom within 4 Å of CR are colored cyan and depicted as ball-stick model. The remaining amino acids of the Aβ(1-42) fibril are colored orange or blue, respectively. Panels at the bottom were rotated by 90° or 75° relative to the ones at the top.

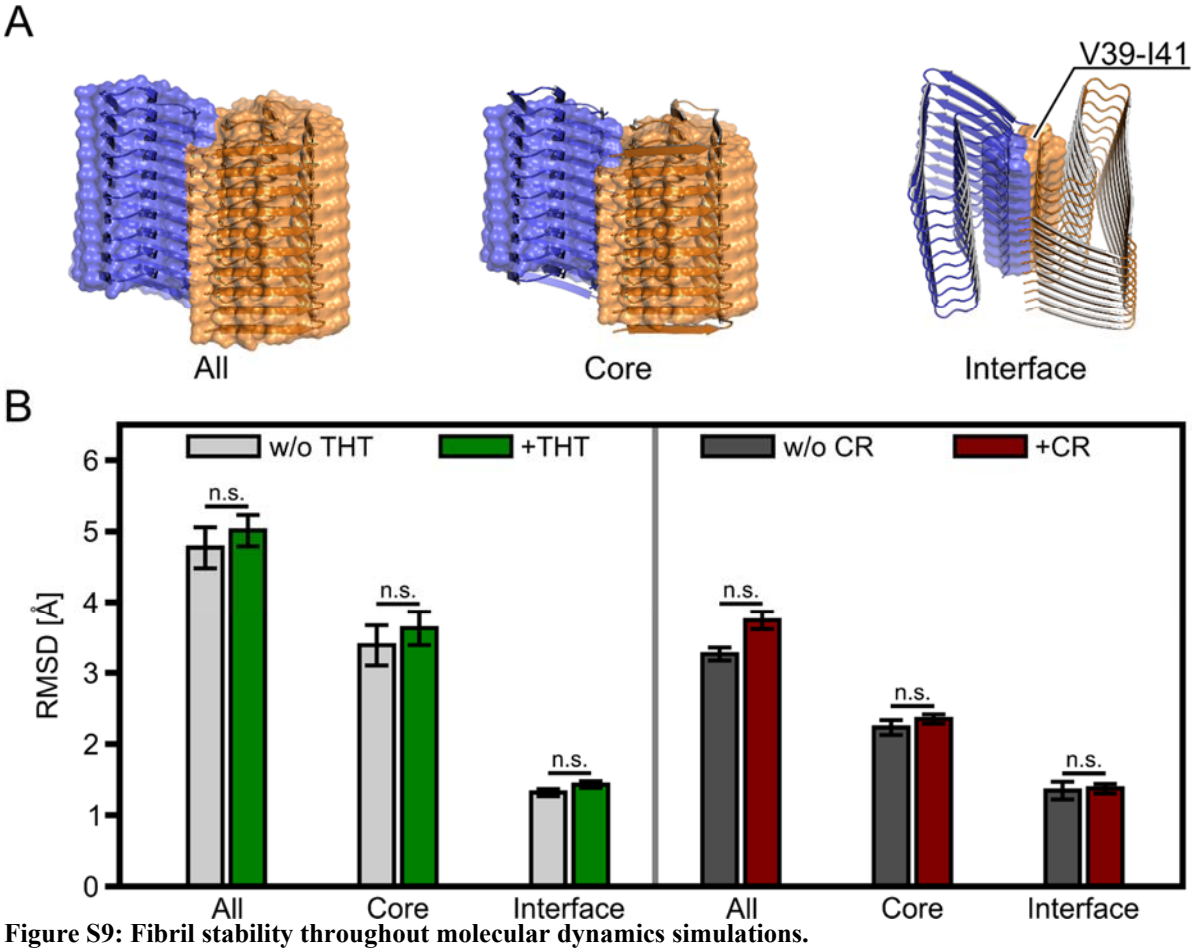

Figure S9: Fibril stability throughout molecular dynamics simulations.
A: Structural elements that were considered for stability evaluation throughout molecular dynamics (MD) simulations. The considered elements are shown as surface-cartoon representation and the remaining parts only as a cartoon. The element denoted as "All" includes all amino acids of the fibril, the "Core" neglects the Aβ(1-42) peptides at the fibril ends, and the "Interface" only includes amino acids V39 – I41 that form the interface between both protofilaments (colored blue or orange). **B:** Average root mean square deviation (RMSD) calculated for the structural elements shown in panel A relative to the starting structure. In the case of Thioflavin-T (THT), the structural model of the Aβ fibril is composed of ten Aβ peptides (**Figure S1A**). However, the definition of All, Core, and Interface is identical. The gray bars show the average RMSD (n = 10) of the fibril in MD simulations in the absence of any dye molecule. The green bars show the average RMSD (n = 45) of the fibril in THT-binding simulations, the red bars show the average RMSD (n = 45) of the fibril in Congo red (CR)-binding simulations. The error bars denote the standard error of the mean (SEM). The average RMSD and SEM were calculated over 10 or 45 replicas of 1 μs length each. n.s. not statistically significant.

A

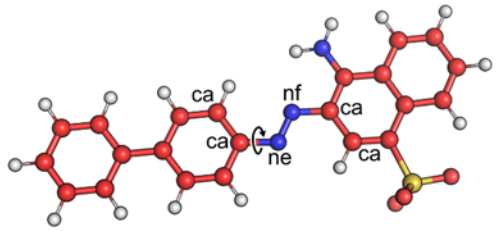

B

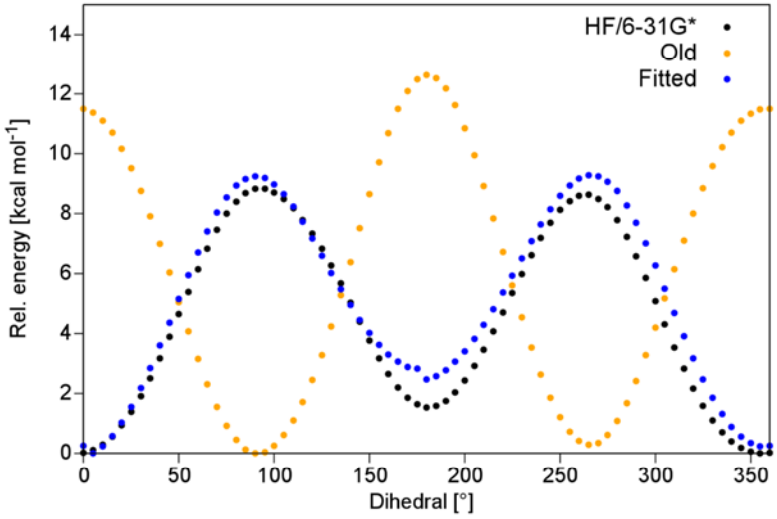

C

Force field parameters for Congo red compatible with GAFF (Version 2.1)

MASS

BOND

ANGLE

oh-s6-ca	41.359	101.710	Calculated with empirical approach	

DIHE

ne-nf-ca-ca	1	-2.9478	87.6658	-0.9802	## paramfit
ne-nf-ca-ca	1	2.9749	175.8314	2.0008	## paramfit
ca-ca-ne-nf	1	-2.9478	87.6658	-0.9802	## paramfit
ca-ca-ne-nf	1	2.9749	175.8314	2.0008	## paramfit

IMPROPER

ca-ca-ca-ha	1.1	180.0	2.0	General improper torsional angle (2 general atom types)
ca-ca-ca-ca	1.1	180.0	2.0	Using default value
ca-ca-ca-s6	1.1	180.0	2.0	Using default value
ca-ca-ca-nh	1.1	180.0	2.0	Using default value
ca-ca-ca-ne	1.1	180.0	2.0	Using default value
ca-ca-ca-nf	1.1	180.0	2.0	Using default value
ca-cp-ca-ha	1.1	180.0	2.0	General improper torsional angle (2 general atom types)
ca-hn-nh-hn	1.1	180.0	2.0	Using default value
ca-ca-cp-cp	1.1	180.0	2.0	Using default value

NONBON

Figure S10: Force field parameters for Congo red.
A: Truncated Congo red (CR) model used to derive the new torsion parameters describing the rotation between the aromatic rings and the diazo group (indicted by the arrow). The labels depict the GAFF atom types. **B:** Potential energy surface scan for torsion angles from 0° to 360° at 5° intervals. Gas phase relative HF/6-31G* energies are shown as black dots, standard GAFF energies as orange dots, and optimized GAFF energies as blue dots. **C:** Extract from the force-field modification file used for MD simulations with CR with parameters compatible with GAFF (version 2.1).

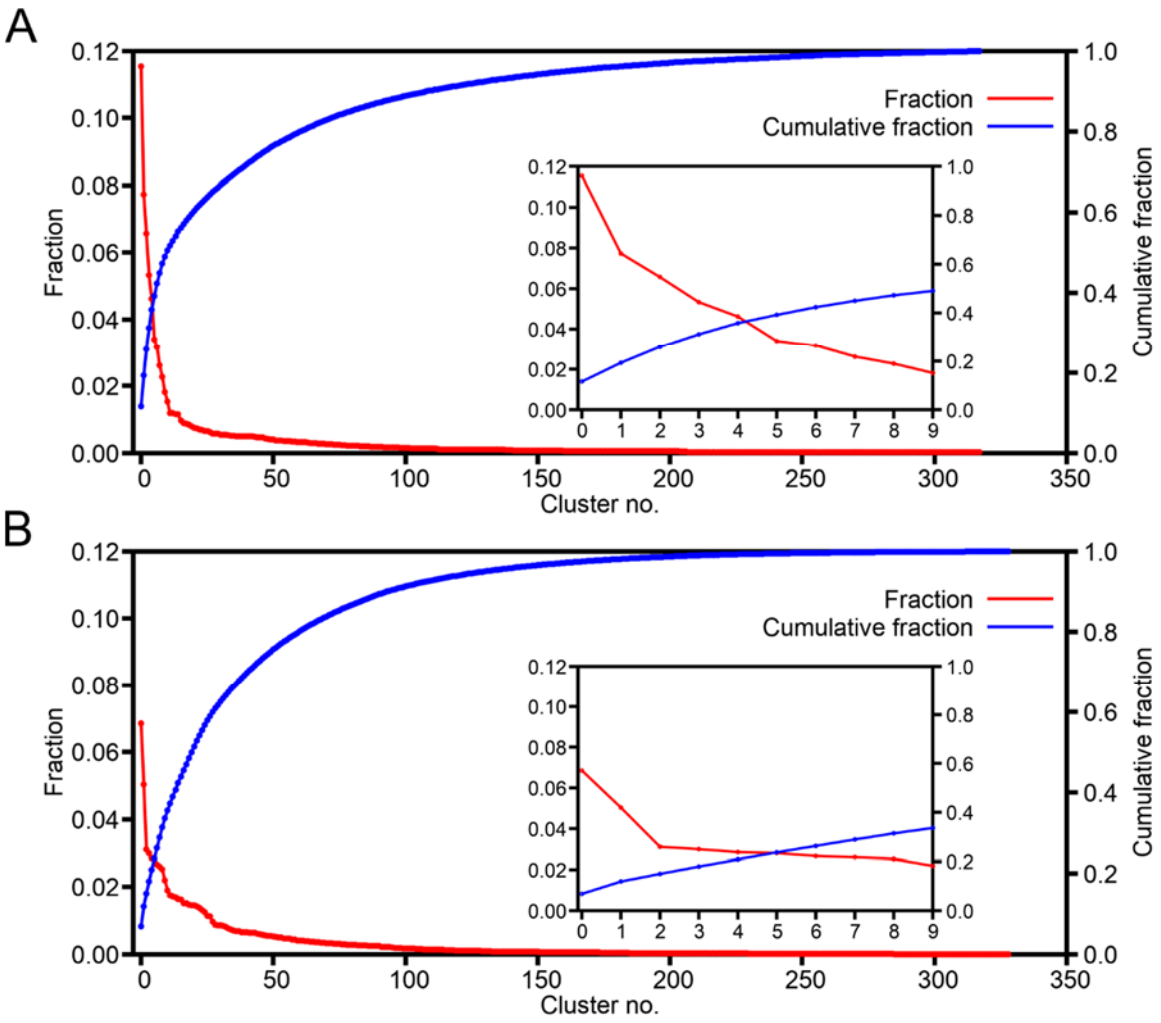

Figure S11: Clustering summary.
Fraction (red line, left y-axis) and cumulative fraction (blue line, right y-axis) of poses per cluster for Thioflavin-T (**A**) and Congo red (**B**). The insets show the ten highest populated clusters (from 0 to 9).

Supplemental Tables

Table S1: Results of hierarchical clustering and MM-GBSA calculations for Thioflavin-T.

Cluster	Fraction	$\Delta G_{\text{eff.}}$ [a]	$SEM_{G_{\text{eff}}}$ [b]	$T \cdot \Delta S_{\text{conf.}}$ [a]	SEM_{TS} [b]	$\Delta G_{\text{bind.}}$ [a]	$\Delta G^{0}_{\text{bind}}$ [a]	SEM_{total} [b]	Lower K_D^{comp} [c]	Upper K_D^{comp} [c]	$K_{D\,(i)}^{\text{exp}}$ [c]
c0	0.12	-25.34	0.07	-18.19	0.33	-7.16	-9.06	0.42	112	470	
c1	0.08	-23.25	0.08	-17.01	0.35	-6.24	-8.14	0.45	505	2331	
c2	0.07	-23.80	0.09	-16.84	2.03	-6.96	-8.86	2.05	10	10183	
c3	0.05	-24.91	0.12	-18.44	0.39	-6.47	-8.37	0.52	305	1758	665 [42]
c4	0.05	-24.99	0.13	-19.32	0.64	-5.67	-7.57	0.74	820	9830	
c5	0.03	-22.67	0.12	-16.71	0.72	-5.96	-7.86	0.80	445	6676	294 - 4000 [43]
c6	0.03	-24.13	0.18	-18.40	3.23	-5.72	-7.62	3.26	10	634142	
c7	0.03	-22.78	0.13	-17.20	0.75	-5.58	-7.48	0.83	799	13382	
c8	0.02	-20.27	0.14	-15.60	0.51	-4.68	-6.58	0.63	5209	43854	
c9	0.02	-23.22	0.16	-17.70	0.97	-5.52	-7.42	1.05	614	21488	

[a] In kcal mol^{-1}.

[b] Standard error of the mean (SEM) in kcal mol^{-1}.

[c] K_D^{comp} and $K_{D\,(i)}^{\text{exp}}$ are reported in nM. If K_D^{comp} is in agreement with $K_{D\,(i)}^{\text{exp}}$, the cells are colored gray.

Table S2: Results of hierarchical clustering and MM-GBSA calculations for Congo red.

Cluster	Fraction	$\Delta G_{\text{eff.}}$ [a]	$SEM_{G_{\text{eff}}}$ [b]	$T \cdot \Delta S_{\text{conf.}}$ [a]	SEM_{TS} [b]	$\Delta G_{\text{bind.}}$ [a]	$\Delta G^{0}_{\text{bind}}$ [a]	SEM_{total} [b]	Lower K_D^{comp} [c]	Upper K_D^{comp} [c]	$K_{D\,(i)}^{\text{exp}}$ [c]
c0	0.07	-24.16	0.07	-26.07	1.01	1.91	0.01	1.05	-	-	
c1	0.05	-27.84	0.12	-27.92	1.00	0.08	-1.82	1.05	-	-	
c2	0.03	-16.67	0.12	-27.53	1.34	10.87	8.97	1.38	-	-	
c3	0.03	-36.80	0.12	-27.63	1.27	-9.17	-11.07	1.31	0.8	70	
c4	0.03	-35.91	0.18	-23.43	1.91	-12.48	-14.38	1.95	< 0.01	0.8	209 - 3070[44]
c5	0.03	-24.45	0.12	-27.53	1.33	3.08	1.18	1.38	-	-	
c6	0.03	-25.88	0.10	-26.70	1.79	0.81	-1.09	1.82	-	-	
c7	0.03	-32.40	0.18	-24.52	1.77	-7.88	-9.78	1.82	3	1458	
c8	0.03	-18.65	0.08	-26.87	1.45	8.22	6.32	1.48	-	-	
c9	0.02	-22.55	0.07	-21.51	1.73	-1.04	-2.94	1.75	-	-	

[a] In kcal mol^{-1}.

[b] Standard error of the mean (SEM) in kcal mol^{-1}.

[c] K_D^{comp} and $K_{D\,(i)}^{\text{exp}}$ are reported in nM. If K_D^{comp} is in agreement with $K_{D\,(i)}^{\text{exp}}$, the cells are colored gray.

Table S3: Protonation states of titratable amino acids in Aβ(1-42) at pH 2.[a]

Residue ID	Netto charge	Amber residue name
Aspartate 1	-1	ASP
Glutamate 3	0	GLH
Histidine 6	+1	HIP
Aspartate 7	-1	ASP
Glutamate 11	-1	GLU
Histidine 13	+1	HIP
Histidine 14	+1	HIP
Glutamate 22	-1	GLU
Aspartate 23	0	ASH

[a] Taken from ref. 1 and considered in the MD simulations.

Supplemental Movies

Movie S1: Thioflavin-T binding to the amyloid-β(1-42) fibril.
The movie shows the first 500 ns of a representative trajectory (marked by a "*" in Fig. S1) of Thioflavin-T (THT) binding to the amyloid-β(1-42) fibril. THT is shown as green-sphere model, and the amyloid-β(1-42) fibril in surface representation, with both protofilaments colored either blue or orange.

Movie S2: Congo red binding to the amyloid-β(1-42) fibril.
The movie shows the first 500 ns of a representative trajectory (marked by a "*" in Fig. S2) of Congo red (CR) binding to the amyloid-β(1-42) fibril. CR is shown as red-sphere model, and the amyloid-β(1-42) fibril in surface representation, with both protofilaments colored either blue or orange.

Supplemental References

1. L. Gremer, D. Schölzel, C. Schenk, E. Reinartz, J. Labahn, R. B. G. Ravelli, M. Tusche, C. Lopez-Iglesias, W. Hoyer, H. Heise, D. Willbold and G. F. Schröder, *Science*, 2017, **358**, 116-119.
2. L. Schrödinger, *Schrödinger, LLC, New York, NY*, 2017.
3. J. C. Shelley, A. Cholleti, L. L. Frye, J. R. Greenwood, M. R. Timlin and M. Uchimaya, *J. Comput.-Aided. Mol. Des.*, 2007, **21**, 681-691.
4. M. J. Frisch, G. W. Trucks, H. B. Schlegel, G. E. Scuseria, M. A. Robb, J. R. Cheeseman, G. Scalmani, V. Barone, G. A. Petersson, H. Nakatsuji, X. Li, M. Caricato, A. V. Marenich, J. Bloino, B. G. Janesko, R. Gomperts, B. Mennucci, H. P. Hratchian, J. V. Ortiz, A. F. Izmaylov, J. L. Sonnenberg, Williams, F. Ding, F. Lipparini, F. Egidi, J. Goings, B. Peng, A. Petrone, T. Henderson, D. Ranasinghe, V. G. Zakrzewski, J. Gao, N. Rega, G. Zheng, W. Liang, M. Hada, M. Ehara, K. Toyota, R. Fukuda, J. Hasegawa, M. Ishida, T. Nakajima, Y. Honda, O. Kitao, H. Nakai, T. Vreven, K. Throssell, J. A. Montgomery Jr., J. E. Peralta, F. Ogliaro, M. J. Bearpark, J. J. Heyd, E. N. Brothers, K. N. Kudin, V. N. Staroverov, T. A. Keith, R. Kobayashi, J. Normand, K. Raghavachari, A. P. Rendell, J. C. Burant, S. S. Iyengar, J. Tomasi, M. Cossi, J. M. Millam, M. Klene, C. Adamo, R. Cammi, J. W. Ochterski, R. L. Martin, K. Morokuma, O. Farkas, J. B. Foresman and D. J. Fox, *Journal*, 2016.
5. L. Martinez, R. Andrade, E. G. Birgin and J. M. Martinez, *J. Comput. Chem.*, 2009, **30**, 2157-2164.
6. W. L. Jorgensen, J. Chandrasekhar, J. D. Madura, R. W. Impey and M. L. Klein, *J. Chem. Phys.*, 1983, **79**, 926-935.
7. C. E. A. F. Schafmeister, W. S. Ross and V. Romanovski, *University of California, San Francisco*, 1995.
8. D. A. Case, R. M. Betz, W. Botello-Smith, D. S. Cerutti, T. E. Cheatham III, T. A. Darden, R. E. Duke, T. J. Giese, H. Gohlke, A. W. Goetz, N. Homeyer, S. Izadi, P. Janowski, J. Kaus, A. Kovalenko, T. S. Lee, S. LeGrand, P. Li, C. Lin, T. Luchko, R. Luo, B. Madej, D. Mermelstein, K. M. Merz, G. Monard, H. Nguyen, H. T. Nguyen, I. Omelyan, A. Onufriev, D. R. Roe, A. Roitberg, C. Sagui, C. L. Simmerling, J. Swails, R. C. Walker, J. Wang, R. M. Wolf, X. Wu, L. Xiao, D. M. York and P. A. Kollman, *University of California, San Francisco.*, 2016.
9. J. A. Maier, C. Martinez, K. Kasavajhala, L. Wickstrom, K. E. Hauser and C. Simmerling, *J. Chem. Theory Comput.*, 2015, **11**, 3696-3713.
10. J. M. Wang, R. M. Wolf, J. W. Caldwell, P. A. Kollman and D. A. Case, *J. Comput. Chem.*, 2004, **25**, 1157-1174.
11. W. D. Cornell, P. Cieplak, C. I. Bayly and P. A. Kollman, *J. Am. Chem. Soc.*, 1993, **115**, 9620-9631.
12. C. I. Bayly, P. Cieplak, W. D. Cornell and P. A. Kollman, *J. Phys. Chem.*, 1993, **97**, 10269-10280.
13. C. Wu, Z. X. Wang, H. X. Lei, W. Zhang and Y. Duan, *J. Am. Chem. Soc.*, 2007, **129**, 1225-1232.
14. R. M. Betz and R. C. Walker, *J. Comput. Chem.*, 2015, **36**, 79-87.
15. B. Frieg, B. Görg, N. Homeyer, V. Keitel, D. Häussinger and H. Gohlke, *PLoS Comput. Biol.*, 2016, **12**, e1004693.
16. S. Bhatia, D. Diedrich, B. Frieg, H. Ahlert, S. Stein, B. Bopp, F. Lang, T. Zang, T. Kroger, T. Ernst, G. Kogler, A. Krieg, S. Ludeke, H. Kunkel, A. J. Rodrigues Moita, M. U. Kassack, V. Marquardt, F. V. Opitz, M. Oldenburg, M. Remke, F. Babor, M. Grez, A. Hochhaus, A. Borkhardt, G. Groth, L. Nagel-Steger, J. Jose, T. Kurz, H. Gohlke, F. K. Hansen and J. Hauer, *Blood*, 2018, **132**, 307-320.
17. B. Frieg, D. Häussinger and H. Gohlke, in *Proceedings of the NIC Symposium 2016*, eds. K. Binder, M. Müller, M. Kremer and A. Schnurpfeil, Jülich, 2016, pp. 97-104.
18. T. Darden, D. M. York and L. G. Pedersen, *J. Chem. Phys.*, 1993, **98**, 10089-10092.
19. R. Salomon-Ferrer, A. W. Götz, D. Poole, S. Le Grand and R. C. Walker, *J. Chem. Theory Comput.*, 2013, **9**, 3878-3888.
20. D. Krause, *JLSRF*, 2019, **5**, A135.
21. C. W. Hopkins, S. Le Grand, R. C. Walker and A. E. Roitberg, *J. Chem. Theory Comput.*, 2015, **11**, 1864-1874.
22. D. R. Roe and T. E. Cheatham III, *J. Chem. Theory Comput.*, 2013, **9**, 3084-3095.
23. K. L. Kostka, M. D. Radcliffe and E. Vonmeerwall, *J. Phys. Chem.*, 1992, **96**, 2289-2292.
24. M. K. Inglesby and S. H. Zeronian, *Dyes Pigm.*, 2001, **50**, 3-11.
25. C. Wu, M. T. Bowers and J. E. Shea, *Biophys J*, 2011, **100**, 1316-1324.
26. C. Wu, J. Scott and J. E. Shea, *Biophys J*, 2012, **103**, 550-557.
27. J. Y. Shao, S. W. Tanner, N. Thompson and T. E. Cheatham III, *J. Chem. Theory Comput.*, 2007, **3**, 2312-2334.
28. B. R. Miller, T. D. McGee, J. M. Swails, N. Homeyer, H. Gohlke and A. E. Roitberg, *J. Chem. Theory Comput.*, 2012, **8**, 3314-3321.
29. H. Gohlke and D. A. Case, *J. Comput. Chem.*, 2004, **25**, 238-250.
30. N. Homeyer, F. Stoll, A. Hillisch and H. Gohlke, *J. Chem. Theory Comput.*, 2014, **10**, 3331–3344.
31. S. Genheden and U. Ryde, *Expert. Opin. Drug. Dis.*, 2015, **10**, 449-461.
32. T. Hou, J. Wang, Y. Li and W. Wang, *J. Chem. Inf. Model.*, 2011, **51**, 69-82.

33. T. Hou, J. M. Wang, Y. Y. Li and W. Wang, *J. Comput. Chem.*, 2011, **32**, 866-877.
34. N. Homeyer and H. Gohlke, *Mol. Inf.*, 2012, **31**, 114-122.
35. I. J. General, *J. Chem. Theory Comput.*, 2010, **6**, 2520-2524.
36. D. A. McQuarrie, *Statistical mechanics*, Harper & Row, New York, 1976.
37. J. Janin, *Proteins: Struct., Funct., Genet.*, 1996, **25**, 438-445.
38. M. K. Gilson, J. A. Given, B. L. Bush and J. A. McCammon, *Biophys J*, 1997, **72**, 1047-1069.
39. H. B. Luo and K. Sharp, *Proc. Natl. Acad. Sci. U. S. A.*, 2002, **99**, 10399-10404.
40. H. Gohlke, C. Kiel and D. A. Case, *J. Mol. Biol.*, 2003, **330**, 891-913.
41. A. I. Sulatskaya, A. A. Maskevich, I. M. Kuznetsova, V. N. Uversky and K. K. Turoverov, *PLoS One*, 2010, **5**.
42. J. Zhang, A. Sandberg, A. Konsmo, X. Y. Wu, S. Nystrom, K. P. R. Nilsson, P. Konradsson, H. LeVine, M. Lindgren and P. Hammarstrom, *Chem. - Eur. J.*, 2018, **24**, 7210-7216.
43. Z. P. Zhuang, M. P. Kung, C. Hou, D. M. Skovronsky, T. L. Gur, K. Plossl, J. Q. Trojanowski, V. M. Y. Lee and H. F. Kung, *J. Med. Chem.*, 2001, **44**, 1905-1914.
44. M. Stravalaci, M. Beeg, M. Salmona and M. Gobbi, *Biosens Bioelectron*, 2011, **26**, 2772-2775.